Korean J. Chem. Eng., 37(12), 2117-2123 (2020)
DOI: 10.1007/s11814-020-0656-5

pISSN: 0256-1115
eISSN: 1975-7220

Direct numerical simulation of microbubble streaming in a microfluidic device: The effect of the bubble protrusion depth on the vortex pattern

Behrouz Behdani[*,], Saman Monjezi[*], Jie Zhang[***], Cheng Wang[***,†], and Joontaek Park[*,****,†]**

*The Department of Chemical and Biochemical Engineering, Missouri University of Science and Technology, Rolla, MO 65409, USA
**The Department of Chemical and Biomolecular Engineering, Vanderbilt University, Nashville, TN 37212, USA
***The Department of Mechanical and Aerospace Engineering, Missouri University of Science and Technology, Rolla, MO 65409, USA
****The Biomedical, Biological and Chemical Engineering Department, University of Missouri, Columbia, MO 65211, USA
(*Received 21 April 2020 • Revised 27 July 2020 • Accepted 5 August 2020*)

Abstract−Microbubble streaming in a microfluidic device has been increasingly studied and used in recent years, due to its unique flow pattern that can promote mixing, sort particles and trap particles in microscale flows. However, there have been few numerical studies of this subject. We performed a 3D direct simulation of a cylindrical-shaped microbubble, trapped in a pit of a microchannel and sandwiched between two parallel plates, vibrated by pressure oscillation. Our simulation was able to reproduce the experimentally observed relation between the bubble protrusion depth and the vortex pattern: As the bubble protrusion depth increased, new vortices emerged and grew larger. Our investigation of the streamlines near the bubble interface indicates that the number of non-spherical nodes in the bubble interface is closely related to the flow pattern in the liquid phase. It was also validated by our simulation that the flow velocity showed an exponentially decaying trend as the radial distance outward from the vortex center. Our numerical model was also used to investigate the effects of surface tension and channel size on the vortex pattern. Larger surface tension or smaller channel size showed a similar effect as the increased protrusion depth induced more vortices.

Keywords: Acoustic Bubble Streaming, Oscillating Bubble, Microfluidics, Numerical Modeling, Multiphase Flow

INTRODUCTION

Microbubble streaming is a phenomenon where a micro-sized bubble is vibrated by acoustic pressure, resulting in steady vortical flows around the bubble [1,2]. During the last decade, microbubble streaming flows has emerged as a powerful technique for actuating fluids in microfluidics. More than just fluid transport [3-5], these tiny vibrating bubbles can mix fluid at microscale [6-8], sort and trap particles [9,10] and biomolecules [11-20], generate chemical gradients [6], power micro-swimmers [7,21], and generate micro-droplets [22].

Due to these successful applications, fundamental studies to investigate the origin of the vortex pattern have been carried out. Theoretical modeling has been done on a spherical microbubble vibrating in an infinite medium [23-25]. However, studies on the particularly relevant microfluidic system, a cylindrical bubble trapped in a pit of a microchannel, are necessary for further development and optimized performance for the abovementioned applications. Experimental and theoretical studies of the frequency effect on bubble vibration dynamics and vortex patterns were performed: It was found that as the driving frequency increases, higher order vibration modes become dominant and lead to different streaming flows. The eventual streaming flows are the result of a combination of the bubble induced streaming and wall induced streaming [26,27]. Another study reported that the stability of the trapped bubble is affected by the difference between the surrounding air pressure and the bubble pressure. Therefore, temperature and humidity of the surrounding must be controlled to be constant for reproducible experimental results [28]. A subsequent study investigated the effect of the bubble protrusion depth in the liquid channel on the vortex pattern [29]. As the protrusion depth is varied, the oscillation mode of the bubble is changed causing different vortex patterns.

In this study, we validated and performed a direct 3D simulation of a cylindrical microbubble vibrated by pressure oscillation to investigate the protrusion depth effect on the vortex pattern. The bubble protrusion depth was controlled by the difference of the pressure between the main and the side microchannels. We also investigated the effects of surface tension and channel size on the vortex pattern. To the best of our knowledge, there are no studies that have used direct numerical simulation to study microbubble streaming in a realistic microfluidic device similar to those used in prior experimental applications.

SIMULATION METHOD

1. Governing Equation

To describe the flows induced by a vibrating bubble, mass and momentum equations are used to model the dynamics of the two

†To whom correspondence should be addressed.
E-mail: wancheng@mst.edu, parkjoon@missouri.edu

Table 1. Simulation parameters

Parameters	Nomenclature	Values	Units
P_g	Side edge gauge pressure	2,120	Pa
P_l	Main edge gauge pressure	1,200-2,000	Pa
a	Radius of side channel	40	μm
d	Protrusion depth of bubble	20-56	μm
σ	Surface tension	0.01-0.05	N/m
ρ_l	Liquid density	1,050	kg/m^3
ρ_g	Bubble density	1.189	kg/m^3
μ_l	Liquid viscosity	0.005	Pa·s
μ_g	Bubble viscosity	1.81×10^{-5}	Pa·s

phase (gas and liquid) system.

$$\frac{\partial \rho}{\partial t}+\nabla\cdot(\rho\mathbf{u})=0 \tag{1}$$

$$\frac{\partial(\rho\mathbf{u})}{\partial t}+\nabla\cdot(\rho\mathbf{u}\mathbf{u})=-\nabla p+\mu\nabla^2\mathbf{u}+\rho\mathbf{g} \tag{2}$$

Here, ρ, **u**, p, and μ are the density, velocity vector, pressure, and dynamic viscosity, respectively, of the fluid in each phase. At the interface, a surface tension body force, $\sigma\nabla\cdot(\nabla\alpha/|\nabla\alpha|)\nabla\alpha$ (σ is a surface tension and α is a liquid fraction, which will be defined later), is added on the right-hand side of Eq. (2). In the simulation, it was assumed that the density of each phase remained constant. Since the Reynolds number, $\mathrm{Re}=a^2\omega\rho/\mu$ (see Table 1 for notations and values), of this system is less than 100, a turbulence model is not required.

For the simulation of a multiphase system, the volume of fluid (VOF) approach was chosen. Since VOF is a Eulerian approach, a color function at a position, **x**, and a time, t, is defined as:

$$\phi(\mathbf{x},t)=\begin{cases}1 \text{ for } \mathbf{x}\in D_l \text{ at time t}\\ 0 \text{ for } \mathbf{x}\in D_g \text{ at time t}\end{cases} \tag{3}$$

where D_l and D_g indicate the domains of liquid and gas phases, respectively. The liquid fraction of the *i*-th cell, located at $\mathbf{x}_i$ and t, is evaluated by taking the average of $\phi(\mathbf{x}, t)$ over the volume of a cell:

$$\alpha(\mathbf{x}_i,t)=\frac{1}{V_{cell}}\int_{V_{cell}}\phi(\mathbf{x},t)dV. \tag{4}$$

Phase-average density at each **x** and t is calculated as:

$$\rho(\mathbf{x},t)=\rho_l\phi(\mathbf{x},t)+\rho_g(1-\phi(\mathbf{x},t)). \tag{5}$$

The density terms in Eq. (1) are replaced with Eq. (5) and subsequently Eq. (4) is applied using the Leibniz integral rule to give an equation that describes the dynamics of the liquid fraction:

$$\frac{\partial\alpha}{\partial t}+\nabla\cdot(\alpha\mathbf{u})=0. \tag{6}$$

2. Numerical Implementation

The governing Eqs. (1)-(6) were numerically solved utilizing OpenFOAM, an open source CFD software, based on the finite volume method. Various modules, based on object-oriented programming for solving many different computational fluid dynamics (CFD) problems are available online [30]. For our study, we chose the "InterFOAM" module, which was developed for simulating incompressible isothermal immiscible fluids based on VOF. Since the bubble deformation is small compared to the bubble size, incompressible fluid assumptions for both phases are enough. The InterFOAM solver has been validated for resolving numerical errors, such as loss of volume or nonphysical currents, associated with VOF method in bubble simulations by introducing the approaches of interface sharpening and VOF smoothing [31,32]. Additionally, the InterFOAM was recently modified to be extended to a non-isothermal multiphase flow simulation to give improved agreement with experimental data [33].

Fig. 1 depicts the microfluidic system of our study. The system consists of the main channel with L=3,000 μm (channel length) and H=320 μm (channel height) and the side channel with a width of 2a=80 μm, which is connected and open at the center of the bottom wall of the main channel. The channel depth is 100 μm. It was experimentally confirmed that the bubble forms a cylindrical shape in this condition [34]. It is noted that we performed 3D simulation but only the *xy*-plane view is shown (the horizontal direction and the vertical direction in Fig. 1 are set as the *x*- and the *y*-direction, respectively). There is a finding that the acoustic bubble streaming is a 3D phenomenon and cannot be assumed as a 2D

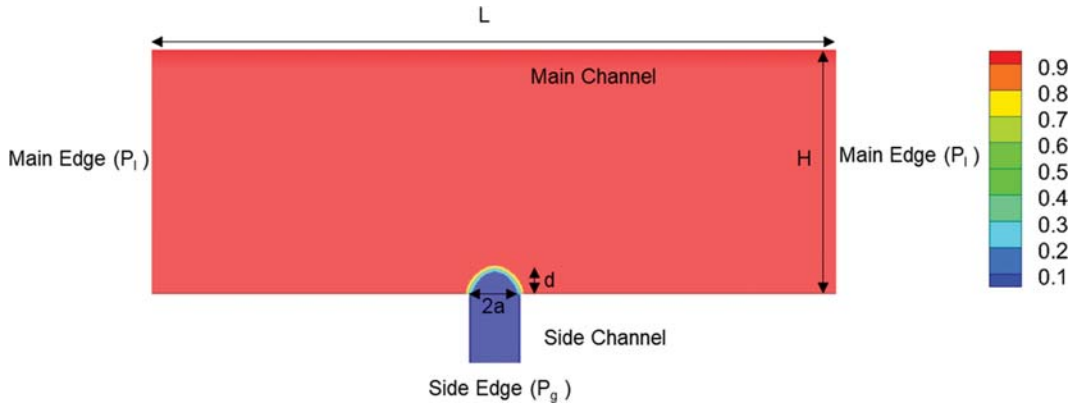

Fig. 1. Schematic diagram of the microfluidic system in the view of xy plane: The color bar indicates the liquid fraction, α. The main channel is filled with a liquid (α=1) and a bubble (α=0) is trapped in the side channel.

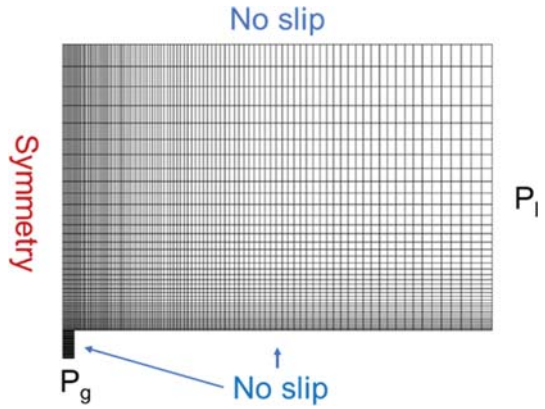

Fig. 2. Meshing of the simulation domain: symmetry boundary condition is applied on the left side. No slip boundary condition is imposed on all the walls. Pressures are imposed on the channel edges (inlets) as in Table 1.

phenomenon in a confined system [35]. The main channel is mostly filled with a liquid while a bubble is trapped in the side channel. The properties of each phase are summarized in Table 1. A no-slip boundary condition is imposed on all of the channel walls except for the edges (inlets) of each channel, zero stress boundary condition is imposed.

Fig. 2 shows the simulation meshes with 48,000 hexahedral grids. Our grid tests showed that meshed finer than 30,000 grids did not give significant differences in the results. To reduce the computational load, a symmetry boundary condition is applied so that only half of the system geometry should be simulated. Finer grids are applied near the side channel entrance to the main channel, where the protruded bubble vibrates. We chose a time-step size of 10^{-6} s based on Courant number at each cell and did not give noticeable changes in smaller time-step sizes.

Initially, before the bubble starts vibrating, the main channel is filled with the liquid and the side channel is filled with the gas. By imposing the pressure on the side channel edge (P_g=2,120 Pa) and both main edges (P_l=1,200 Pa), the bubble protrudes into the main channel, as shown in Fig. 1.

The protrusion depth of the bubble, d, can be controlled by adjusting P_l. However, if P_l is either too large or too small, the liquid will flow into the side channel or the gas will flow into the main channel without forming a bubble. We managed to find P_l to maintain a protruded bubble shape at a given P_g by trial and error. Once the intended protrusion of the bubble is achieved and remains stable, the bubble is vibrated with a frequency, ω, by changing P_g (in gauge pressure) with:

$$P_g = P_{g0} + P^* \sin(\omega t). \quad (7)$$

Here, P_{g0} is a pressure of the bubble used in the initial bubble protrusion and P^* is the perturbation amplitude induced vibration on the bubble surface. We found that any amplitude values between 30 and 100 Pa ensured stable bubble vibration without changing the results. We chose P^*=100 Pa for this study. Under such a driving pressure, the bubble interface oscillates around its equilibrium interface. The flow pattern is obtained by the time-average of the flow velocity components:

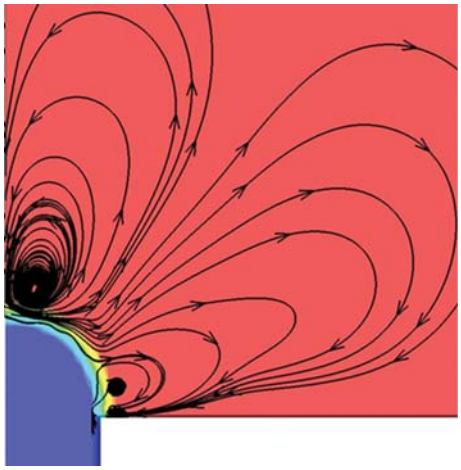

Fig. 3. Flow patterns (average streamlines) at ω=110,000 rad/s and σ=0.05 N/m. Two vortices appear on the right half side of the bubble in the liquid phase.

$$\bar{\mathbf{u}} = \frac{1}{T_2 - T_1} \int_{T_1}^{T_2} \mathbf{u} dt \quad (8)$$

Here, the time-averages were taken over a certain period of time between $t=T_1$ and $t=T_2$. The times T_1 and T_2 were chosen so that the flow pattern was periodically stable. The flow typically reached periodically stable state after a few cycles (typically T_1=0 s and T_2= 0.2 s). One example of the flow pattern is shown in Fig. 3. We are particularly interested in the vortices right next to the bubble. Therefore, the simulation results of the flow pattern are only shown in that region.

It was observed that the magnitude of the continuity equation errors (relative errors of volume between each iteration step) in each cell as well as in the whole domains was maintained less than 6×10^{-7} from the bubble formation to the vortex stabilization, which also indicates that the InterFOAM properly solved the governing equations.

RESULTS AND DISCUSSION

1. The Bubble Protrusion Effect

The bubble protrusion effect on the streaming flow pattern was investigated by performing the simulations while varying d by controlling P_l as shown in Table 1. Fig. 4 shows the simulated flow patterns with respect to different values of d. In the low protrusion of d=20 μm, only one vortex appeared on the right half side of the bubble. The flow direction of the vortex was found to be clockwise. In the medium protrusion of d=30 μm, another small vortex right above the bubble emerged. The second vortex had a counter-clockwise flow direction. As d increased to 53 μm, the second vortex became larger. The change of vortex pattern was associated with the dynamic modes of the bubble surface and competition between streaming flows induced by the solid horizontal wall and the vibrating microbubble [34].

The trend of the flow pattern depending on d is consistent with the experimental observation. Volk and Kahler experimentally investigated the protrusion effect on the flow pattern [29]. We performed

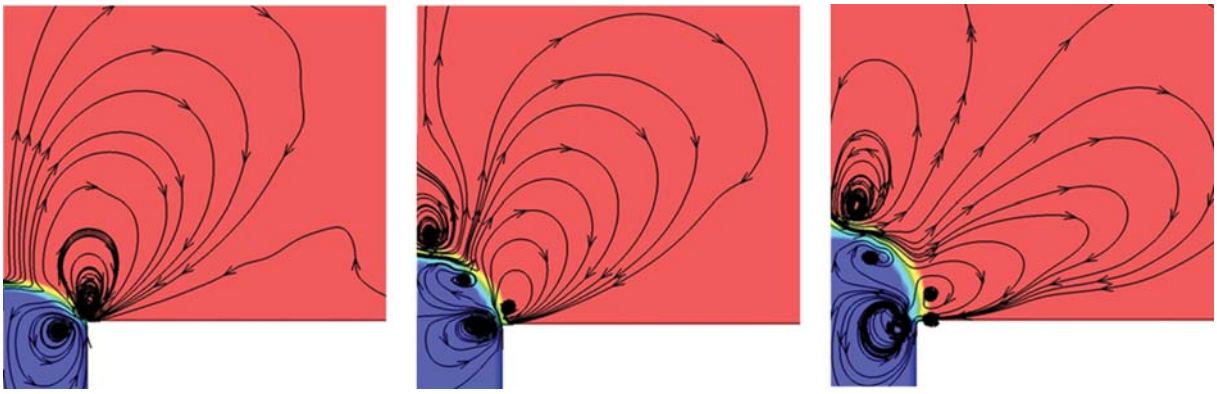

Fig. 4. The effect of protrusion, d, on the flow patterns (σ=0.05 N/m, ω=110,000 rad/s). As the protrusion of the bubble in the main channel (d/a=0.5, 0.75, and 1.325 from left to right respectively) increases, another vortex appears and its size becomes larger.

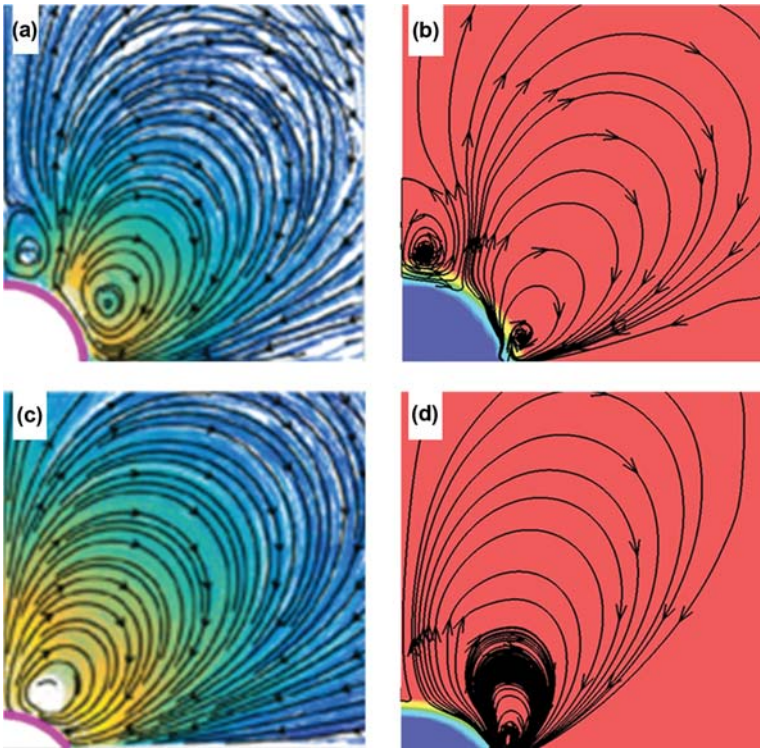

Fig. 5. Comparison of simulation results with the experimental results by Volk and Kahler [29] [ω=22,000 rad/s, d/a=1.36 (a) and 0.67 (c) for the experiments, and d/a=1.31 (b) and 0.73 (d) for the simulations] [The experimental images were adapted from Volk and Kahler [29] by permission from American Physical Society].

the simulation with the similar conditions to those used in Volk and Kahler's experiments, including the protrusion size. The simulation results are compared with the experimental data in Fig. 5. The number, shape, and the flow directions of vortices observed in the experiment match the simulation results.

We investigated the streamlines of the both liquid and gas phases near the bubble surface to rationalize the origin of the protrusion effect on the flow pattern. Fig. 6 shows the simulated streamlines of the both gas and liquid phases for different protrusions. For the lower protrusion, one vortex appears in the gas phase that looks like a mirror image of the vortex in the liquid phase. For the higher protrusion, two vortices appear in the gas phase that look like a pairing of the vortices in the liquid phase. Especially for the high protrusion, the streamlines on the bubble interface indicate the existence of vibrating nodes. As the bubble protrusion increases, the extended bubble interface has an increased number of nodes, which induces vortices in the liquid phase. It is also noted that paired vortices in the liquid and gas phases are in the opposite directions. The previous works, including classical ones [23] as well as recent microfluidics related [6-8], also suggested that the flow pattern is related to the dynamics of the bubble interface for both isolated spherical bubbles and sessile semi-cylindrical bubbles.

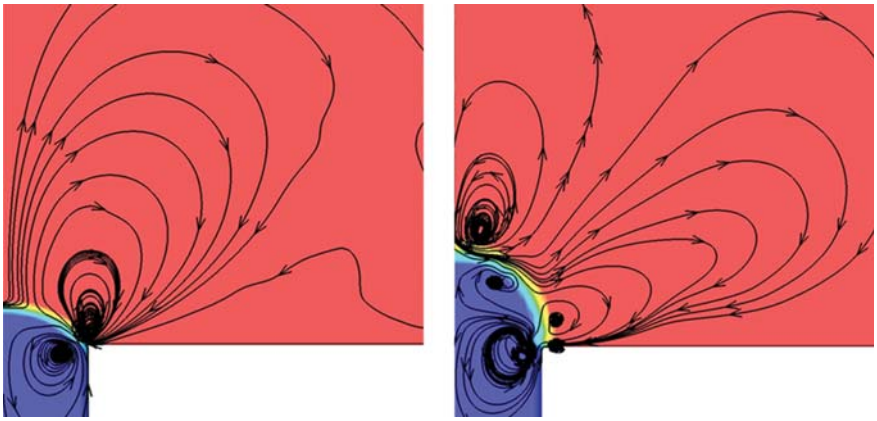

Fig. 6. Magnified views of the simulated streamlines (σ=0.05 N/m, ω=110,000 rad/s) in the both gas and liquid phases near the bubble interface for low (Left: d/a=0.73) and high (Right: d/a=1.325) protrusions. Each vortex in the liquid phase has its pair in the bubble phase.

Volk and Kahler also experimentally measured flow velocity as a function of a radial distance from the vortex center using particle tracing techniques. The experimental results showed a trend that the flow velocity decays with an approximate exponent of −0.016 for all measured protrusions [29]. We compared the exponent from our simulations with similar protrusions to the experimental data in Fig. 7. Considering that the observed exponent −0.016 was averaged from fluctuating experimental data, the simulated trend shows fairly good agreement with the experimental exponent.

2. Surface Tension Effect

In the pinched bubble, bubble pressure, liquid pressure, and surface tension are in equilibrium. Therefore, the surface tension also plays an important role in the bubble protrusion. The variation of surface tension is of practical importance, as its value can be intentionally adjusted with surfactants or accidently by contamination. We investigated the effect of surface tension on the flow patterns. We maintained the bubble protrusion at the maximum possible pressure difference between P_g and P_l. At this pressure difference, the bubble protrusion is also maintained at its maximum. If the pressure difference grows larger, the bubble keeps growing to the main channel and not pinched in the side channel. We employed three different surface tensions of σ=0.01, 0.03, and 0.05 N/m and the results are compared in Fig. 8.

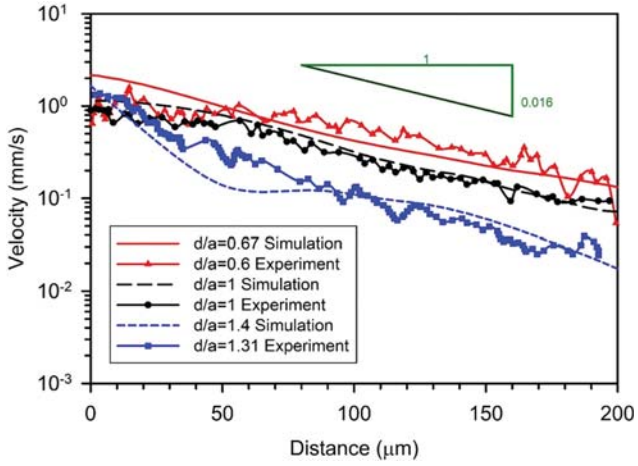

Fig. 7. Flow velocity magnitude as a function of radial distance outward from the vortex center. Results for different protrusions show that exponent is insensitive to the protrusion depth.

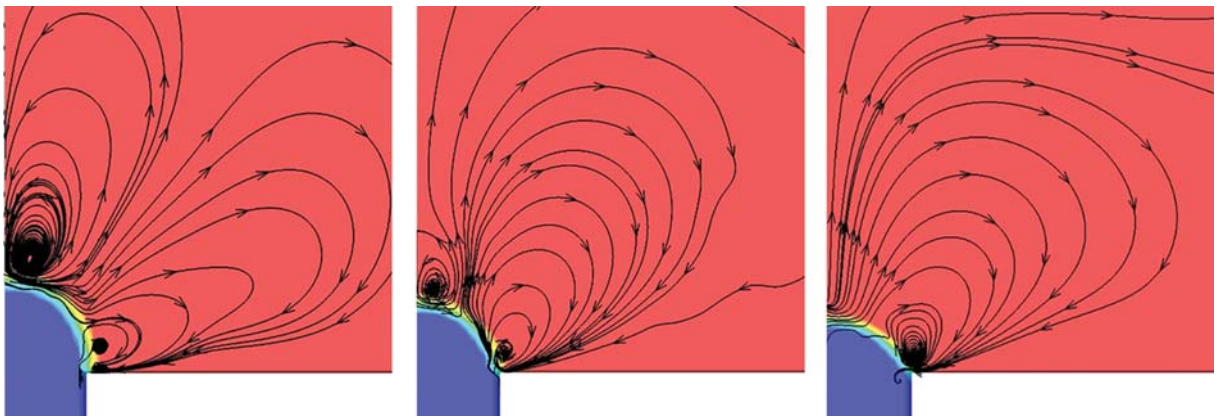

Fig. 8. Effect of surface tension on the vortex pattern. Streamlines were obtained from simulations with different surface tensions (Left: σ=0.05 N/m, Middle: σ=0.03 N/m, and Right: σ=0.01 N/m with the same ω=110,000 rad/s). Pressure conditions are summarized in Table 2. As the surface tension decreases, the size of the vortex on the bubble top decreases.

Table 2. Pressure conditions for the surface tension effect test

σ (N/m)	P_g (Pa)	P_l (Pa)
0.05	2,120	1,200
0.03	2,120	1,550
0.01	2,120	2,000

Table 3. Pressure conditions for the channel size effect test

Main channel size	P_g (Pa)	P_l (Pa)	σ (N/m)
H=700 μm	2,120	1,350	0.05
H=500 μm	2,120	1,280	0.05
H=320 μm	2,120	1,200	0.05

As expected, the higher surface tension of 0.05 N/m can maintain the larger maximum possible pressure difference (shown in Table 2), which results in the maximum possible protrusion, which is enough to produce double vortices, as also shown in Fig. 4. However, the lower surface tension of 0.03 N/m results in the pattern where the second vortex on the bubble is reduced. Even at the lowest surface tension of 0.01 N/m, the second vortex is vanished (a similar trend as in the smaller protrusion). This result indicates a possibility that bubble streaming may be applied to the surface tension measurement in a microfluidic device.

3. The Channel Height Effect

The channel size relative to the bubble size is another practical factor in microfluidics-based applications. It does not only affect the operation throughput but also affects the streaming flows induced by bubbles. Fig. 9 presents the effect of the channel size (height) on flow patterns. Bubble streaming was simulated in the same operating conditions but in different main channel sizes. As in the surface tension test, the bubble was also maintained as the maximum possible pressure difference. The bubble protrusion depth became smaller for smaller channel. Although the number of vortices is the same for each channel, the flow patterns are different: the vortex on the top of the bubble becomes larger in a smaller channel. It can be observed that a narrow channel has a significant distortion effect on the streaming vortex, while the streaming flows in a wide channel look similar to those in unbounded flow.

This phenomenon was also observed in a previous experimental study [34]: The flow characteristics were similar in both the larger and the smaller channels. However, the streaming effect became stronger in a smaller channel while the flow far from the bubble vanished in a larger channel. This is because a closer wall tends to suppress the vortex near the bottom wall, and allows the other vortex to reach to the top wall. A similar phenomenon was also observed that streaming flows induced by an oscillating spherical bubble were intensified near a wall [36]. However, Table 3 shows that the pressure difference became larger for the smaller channel, which implies that the pressure difference change may be another reason for the channel size effect.

CONCLUSION

Our 3D direct simulation of a cylindrical microbubble vibrated by pressure oscillation showed that the increased bubble protrusion depth induces a larger and faster vortex on the top of the bubble and makes the bubble become larger, which matches the experimental observation by Volk and Kahler [29]. Our simulation can also capture the exponentially decreasing decay, similar to the experimentally observed trend of flow velocity decaying in the radial outward direction from the vortex center. Our numerical study demonstrated that the larger surface tension resulted in the increased protrusion depth, which consequently induced a larger vortex. The main channel size effect on the flow pattern was also successfully simulated, which showed qualitative agreement with an experimental study by Wang [34]. The effect of driving frequency and fluid viscoelasticity on the flow pattern is for future study. Our study is expected to contribute to continuing recent advances in microfluidics [37-41].

ACKNOWLEDGEMENT

This work was supported by National Science Foundation (CBET-FD-1901578). JP confirms that BB and SM equally contributed to this work. Authors declare no conflict of interest.

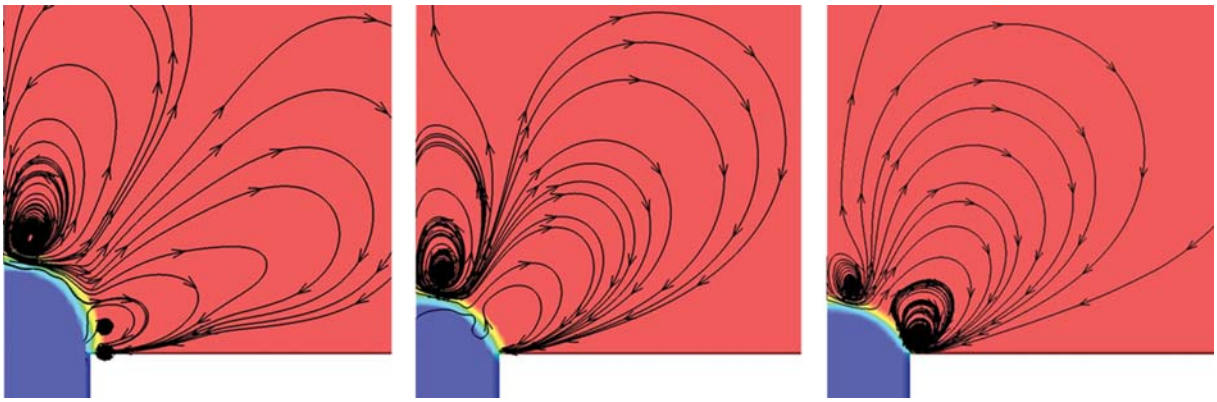

Fig. 9. Effect of the main channel height on the vortex pattern. Streamlines were obtained from simulations with different channel heights, H (Left: H=320 μm, Middle: H=500 μm and Right: H=700 μm with the same σ=0.05 N/m and ω=110,000 rad/s). Pressure conditions are summarized in Table 3. The size of the vortex on the bubble top decreases at a channel with a larger H.

REFERENCES

1. N. Riley, *Theor. Comput. Fluid Dyn.*, **10**, 349 (1998).
2. N. Riley, *Annu. Rev. Fluid Mech.*, **33**, 43 (2001).
3. K. Ryu, S. K. Chung and S. K. Cho, *JALA J. Assoc. Lab. Autom.*, **15**, 163 (2010).
4. P. Marmottant and S. Hilgenfeldt, *Proc. Natl. Acad. Sci.*, **101**, 9523 (2004).
5. A. R. Tovar, M. V Patel and A. P. Lee, *Microfluid. Nanofluidics*, **10**, 1269 (2011).
6. D. Ahmed, C. Y. Chan, S. S. Lin, H. S. Muddana, N. Nama, S. J. Benkovicc and T. J. Huang, *Lab Chip*, **13**, 328 (2013).
7. D. Ahmed, M. Lu, A. Nourhani, P. E. Lammert, Z. Stratton, H. S. Muddana, V. H. Crespi and T. J. Huang, *Sci. Rep.*, **5**, 9744 (2015).
8. B. Rallabandi, C. Wang and S. Hilgenfeldt, *Phys. Rev. Fluids*, **2**, 64501 (2017).
9. S. K. Chung and S. K. Cho, *Microfluid. Nanofluidics*, **6**, 261 (2009).
10. S. K. Chung and S. K. Cho, *J. Micromechanics Microengineering*, **18**, 125024 (2008).
11. C. Wang, S. V Jalikop and S. Hilgenfeldt, *Appl. Phys. Lett.*, **99**, 34101 (2011).
12. S. Monjezi, B. Behdani, M. B. Palaniappan, J. D. Jones and J. Park, *Adv. Chem. Eng. Sci.*, **7**, 362 (2017).
13. R. Zhou and C. Wang, *J. Micromechanics Microengineering*, **25**, 84005 (2015).
14. C. Wang, S. V Jalikop and S. Hilgenfeldt, *Biomicrofluidics*, **6**, 12801 (2012).
15. M. V Patel, A. R. Tovar and A. P. Lee, *Lab Chip*, **12**, 139 (2012).
16. Y. Xie, C. Zhao, Y. Zhao, S. Li, J. Rufo, S. Yang, F. Guob and T. J. Huang, *Lab Chip*, **13**, 1772 (2013).
17. C. Zhao, Y. Xie, Z. Mao, Y. Zhao, J. Rufo, S. Yang, F. Guo, J. D. Maic and T. J. Huang, *Lab Chip*, **14**, 384 (2014).
18. Y. Xie, D. Ahmed, M. I. Lapsley, M. Lu, S. Li and T. J. Huang, *J. Lab. Autom.*, **19**, 137 (2014).
19. M. V Patel, I. A. Nanayakkara, M. G. Simon and A. P. Lee, *Lab Chip*, **14**, 3860 (2014).
20. S. Yazdi and A. M. Ardekani, *Biomicrofluidics*, **6**, 44114 (2012).
21. J. Feng, J. Yuan and S. K. Cho, *Lab Chip*, **15**, 1554 (2015).
22. W.-F. Fang and A. P. Lee, *Microfluid. Nanofluidics*, **18**, 1265 (2015).
23. M. S. Longuet-Higgins, *Proc. R. Soc. London. Ser. A Math. Phys. Eng. Sci.*, **454**, 725 (1998).
24. T. A. Spelman and E. Lauga, *J. Eng. Math.*, **105**, 31 (2017).
25. A. A. Doinikov, S. Cleve, G. Regnault, C. Mauger and C. Inserra, *Phys. Rev. E*, **100**, 33104 (2019).
26. C. Wang, B. Rallabandi and S. Hilgenfeldt, *Phys. Fluids*, **25**, 22002 (2013).
27. B. Rallabandi, C. Wang and S. Hilgenfeldt, *J. Fluid Mech.*, **739**, 57 (2014).
28. A. Volk, M. Rossi, C. J. Kähler, S. Hilgenfeldt and A. Marin, *Lab Chip*, **15**, 4607 (2015).
29. A. Volk and C. J. Kähler, *Phys. Rev. Appl.*, **9**, 54015 (2018).
30. H. Jasak, A. Jemcov and Z. Tukovic, in *International Workshop on Coupled Methods in Numerical Dynamics*, **1000**, 1 (2007).
31. D. A. Hoang, V. van Steijn, L. M. Portela, M. T. Kreutzer and C. R. Kleijn, *Comput. Fluids*, **86**, 28 (2013).
32. S. S. Deshpande, L. Anumolu and M. F. Trujillo, *Comput. Sci. Discov.*, **5**, 14016 (2012).
33. B. Behdani, M. Senter, L. Mason, M. Leu and J. Park, *J. Manuf. Mater. Process.*, **4**, 46 (2020).
34. C. Wang, *Microbubble streaming flows for non-invasive particle manipulation and liquid mixing*, Ph.D. Thesis, University of Illinois at Urbana-Champaign, USA (2014).
35. A. Marin, M. Rossi, B. Rallabandi, C. Wang, S. Hilgenfeldt and C. J. Kähler, *Phys. Rev. Appl.*, **3**, 41001 (2015).
36. A. A. Doinikov and A. Bouakaz, *J. Fluid Mech.*, **742**, 425 (2014).
37. D. Y. Kim and J. M. Kim, *Korean J. Chem. Eng.*, **36**, 837 (2019).
38. P. Ma, T. Fu, C. Zhu and Y. Ma, *Korean J. Chem. Eng.*, **36**, 21 (2019).
39. R. Singh, H.-J. Lee, A. K. Singh and D.-P. Kim, *Korean J. Chem. Eng.*, **33**, 2253 (2016).
40. D. J. Im, *Korean J. Chem. Eng.*, **32**, 1001 (2015).
41. H.-H. Jeong, D. Issadore and D. Lee, *Korean J. Chem. Eng.*, **33**, 1757 (2016).